Energy & Environmental Science

Accepted Manuscript

ROYAL SOCIETY OF CHEMISTRY

www.rsc.org/ees

Thermally Rearranged Polymer Membranes for Desalination

Ji Hoon Kim[1], Sang Hyun Park[1], Moon Joo Lee[2],

Sang Min Lee[1], Won Hyo Lee[1], Kang Hyuck Lee[1],

Na Rae Kang[1], Hye Jin Jo[1], Jeong F. Kim[1],

Enrico Drioli[1, 3, *] and Young Moo Lee[1, 2, *]

[1]Department of Energy Engineering, College of Engineering, Hanyang University, Seoul 133-791, Republic of Korea

[2]Division of Chemical Engineering, College of Engineering, Hanyang University, Seoul 133-791, Republic of Korea

[3]Institute on Membrane Technology (ITM-CNR), University of Calabria, Rende, Cosenza, Italy

***Corresponding authors:**

Y. M. Lee (ymlee@hanyang.ac.kr),

E. Drioli (e.drioli@itm.cnr.it)

Abstract

Herein, we demonstrate thermally-rearranged polybenzoxazole-co-imide (TR-PBOI) electrospun nanocomposite membranes for membrane distillation and membrane crystallization applications. We seek to demonstrate that a synergistic combination of TR polymer, porous nanofibrous membrane, and particle coating improves the long-term stability while maintaining high porosity and water flux. The fabricated membranes exhibit excellent water flux (80 kg $m^{-2} hr^{-1}$) and NaCl rejection (> 99.99 %) with steady performance over more than 186 hours. In addition, for the first time, controlling the heterogeneous nucleation phenomena in membrane crystallization was clearly demonstrated using a TR membrane morphology.

Graphical Abstract

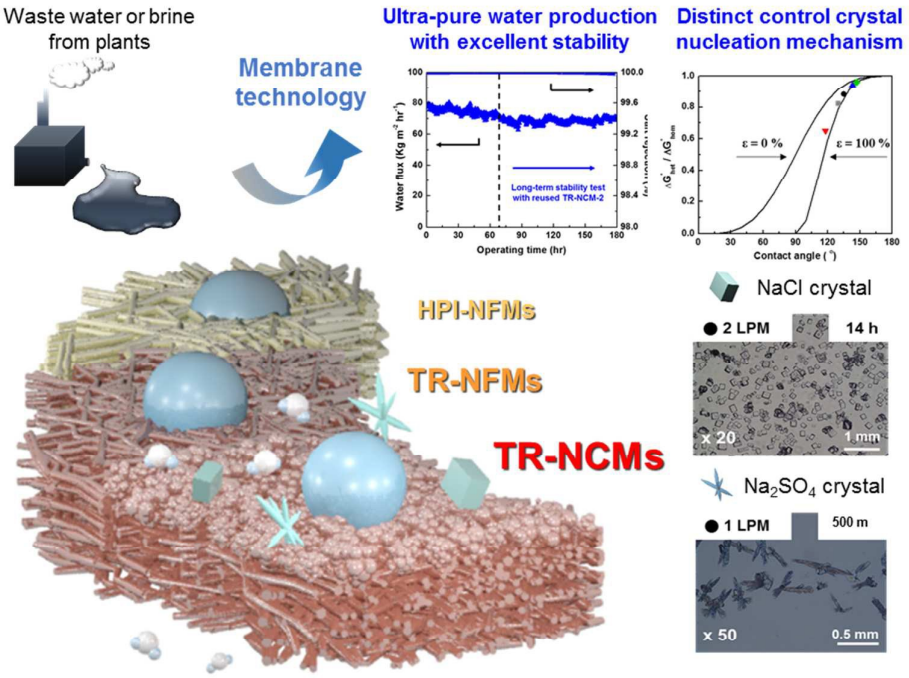

Thermally rearranged polybenzoxazole-co-imide (TR-PBOI) nanofibrous and nanocomposite membranes (NFM and NCM) were developed for membrane distillation and membrane crystallization applications. The TR-PBOI membranes exhibited excellent flux (80 kg m^2 hr^{-1}) and salt rejection (> 99.99 %) over more than 186 hours. These membrane also showed potential for use in membrane crystallization.

Broader Context

Reverse osmosis has been employed to solve the current water crisis because it has high energy efficiency compared with conventional desalination processes. Furthermore, seawater brine is considered as a problematic waste in seawater desalination plants. However, the high osmotic potential and concentrated minerals within the brine may be a fruitful source of energy and resources, which can be conveniently tapped using membrane technology. For instance, the brine can be further concentrated using a membrane distillation (MD) unit to enhance water recovery while increasing the osmotic potential of the brine using low grade energy sources. The concentrated brine can then be routed to a pressure retarded osmosis (PRO) unit or another MD unit to generate electricity, or to a membrane crystallization (MCr) unit to recover valuable minerals such as epsomite and proteins. In this study, we report for the first time the use of thermally-rearranged polybenzoxazole-co-imide (TR-PBOI) nanocomposite membranes in this application. TR-PBOI nanocomposite membranes exhibited stable MD performance with excellent water flux (80 kg m^{-2} h^{-1}) and salt rejection (> 99.99 %) as well as convenient control of crystal nucleation mechanisms. This discovery provides an important addition to the available options for water desalination membranes.

Introduction

Since the membrane distillation (MD) process was first reported in the 1960s, significant improvements have been made in terms of membrane development and process thermodynamic analysis.[1-4] MD process, which is one of the thermally-driven desalination processes, has high energy efficiency, high water flux with excellent salt rejection as well as less fouling phenomena compared with conventional desalination processes, especially at a high feed concentration.[5-7] Optimizing MD performance is a delicate balance between membrane porosity, pore size distribution, thickness, and many other material and process parameters (see **Table S1, ESI†**). However, the current state-of-the-art membranes reported in literature still suffer from one or more drawbacks such as low porosity, wide pore size distribution, low liquid entry pressure (LEP), low water flux, and unstable long-term performance.

Among these drawbacks, long-term stability is the critical challenge that must be resolved in order to industrialize the MD process. Obtaining a high LEP (a threshold pressure at which the liquid begins to penetrate through the membrane) and preventing salt crystallization on the surface pores of a membrane are two particularly important factors for maintaining stable MD performance over a long period of time. Many researchers have developed diverse methodologies such as enhancing the hydrophobicity of the materials, narrowing the pore size distribution, and increasing the surface roughness of the prepared membranes.[8-13]

However, maintaining high water flux and salt rejection over an extended period of time remains a difficult hurdle to overcome in the MD process.

In recent years, electrospun nanofibrous membranes for MD processes have received much attention due to their high porosity (70-90%) and pore connectivity (low tortuosity) compared to the membranes prepared by other means.[5, 14-17] Although electrospun membranes exhibit high flux and rejection, the long-term stability of the membranes was not sufficient for MD operation due to the broad pore size distribution and low LEP. To enhance the LEP of electrospun membranes, composite membranes incorporating inorganic particles such as TiO_2 and SiO_2 have been reported.[8, 10] However, water flux of the composite membranes decreased significantly due to pore blockage, and the particles detached over time from the support membranes. Therefore, recent research in the literature has focused on improving the intrinsic properties of polymers, membrane morphology and post-treatment to fabricate highly porous and hydrophobic membranes with narrow pore size distribution that give a high LEP without compromising water flux and salt rejection.[9, 11-13] (Current state-of-the-art MD membrane performances are summarized in **Table S2, ESI†**.)

Furthermore, membrane crystallization (MCr) has been highlighted as an alternative solution to produce different kinds of crystal products in the pharmaceuticals and fine chemicals industry.[18-21] A unique advantage of the MCr process is the potential to induce heterogeneous nucleation. MCr can reduce the nucleation activation energy and accelerate the nucleation rate at a concentration

lower than the saturation point by trapping the solutes on the surface pores of the membranes. Therefore, it is possible to produce high-quality crystals with high nucleation and growth rates with high process efficiency.[21-23] An ideal MCr membrane should have a uniform pore size distribution and high porosity to produce uniform crystals. In addition, the membrane should also exhibit enough hydrophobicity to nucleate crystals only on the membrane surface pores rather than inside the membrane pores which progressively induce membrane wetting.

Herein, we demonstrate for the first time thermally rearranged polybenzoxazole-co-polyimide (TR-PBOI) nanofibrous membranes for membrane distillation and membrane crystallization applications. TR polymer is intrinsically hydrophobic and can be assembled into various types of porous membranes and nanoparticles.[24, 25] In addition, TR polymer exhibits excellent thermal, chemical, and mechanical stability, and has been reported as a promising candidate for gas separation and lithium ion battery separators.[24, 26, 27] TR nanofibrous and nanocomposite membranes used in battery separator applications have shown excellent thermal and electrochemical stability and outstanding mechanical strength as well as a highly porous and interconnected structure.[27] In this work, we employed a TR polymer precursor, hydroxyl polyimide (HPI). We first fabricated HPI nanofibrous membranes and two types of HPI particles via electrospinning and reprecipitation methods, respectively.

Fig. 1 illustrates the fabrication procedure of TR polymers and nanoparticles and composites thereof. To increase the LEP of the membrane, the surface of the

HPI nanofibrous membrane was first coated with HPI particles. After thermal rearrangement, the HPI nanocomposite membrane chemically rearranged to form a TR-PBOI composite membrane based on the conversion of hydroxyl aromatic imide groups to benzoxazole groups as shown in **Scheme S1, ESI†**. The thermal treatment also resulted in an interconnected structure between the TR nanofibers and particles, which provided a well-defined path for water vapor and excellent mechanical, thermal and chemical stability without any risk of particle detachment. Moreover, the coated TR particles provided a narrow pore size distribution and increased the LEP by capping the large pores on the surface of the electrospun membranes as well as enhanced the surface roughness to reduce the temperature polarization effect.

In this study, we developed two kinds of TR nanofibrous membranes and two different kinds of TR nanocomposite membranes. The effects of hot-pressing and surface coating on the membrane morphology and performances were studied and presented.

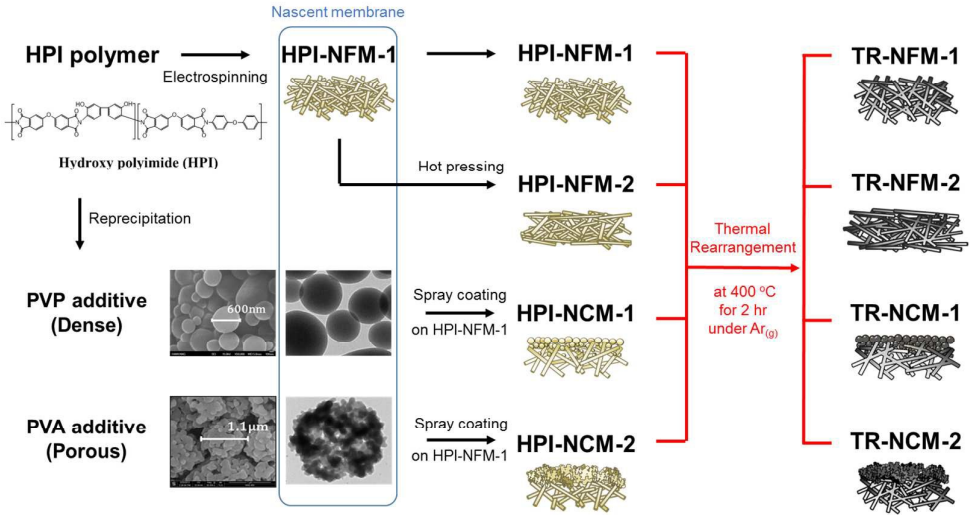

Fig. 1. An illustration of the fabrication of thermally rearranged (TR) polymeric membranes from HPI polymer as a precursor of TR polymer.

Results and discussion

A precursor for TR-PBOI, hydroxy polyimide (HPI), was synthesized using the azeotropic imidization method.[26] The specific procedures used to synthesize the HPI are described in **Scheme S1 (Section S2, ESI†)** and in our previous studies.[26, 27] The synthesized HPI was fabricated into two kinds of HPI nanofibrous membranes (HPI-NFMs) *via* electrospinning (**Section S3, ESI†**) as illustrated in **Fig. 1.** The first membrane was a nascent electrospun membrane, from here on referred to as HPI-NFM-1. The second membrane was made of HPI-NFM-1 that was hot-pressed with 150 kgf.cm^{-2} at 130 ^{o}C, referred to as HPI-NFM-2. We also assembled two types of HPI particles *via* a reprecipitation method using two kinds of additives. The particles made using poly(vinyl alcohol) (PVA, Mw = 85,000) additive exhibited dense spherical shapes, whereas the particles made using poly(vinyl pyrrolidone) (PVP, Mw = 40,000) additive showed a porous sea squirt-like morphology. The role of additives was to stabilize the growing particles and also to facilitate the interaction between the primary particles above the critical aggregation concentration (CAC),[28, 29] inducing the porous sea-squirt shaped particles (specific details are described in **Section S4, ESI†**). Then, each type of HPI particle was dispersed in ethanol (1 *wt*%) and was spray coated onto the surface of HPI-NFM-1 (**Section S5, ESI†**). The membranes coated with PVA-additive and PVP-additive TR particles were named HPI-NCM-1, and HPI-NCM-2, respectively. The thickness of the coating layer was investigated as a function of the sprayed volume to find the appropriate condition that gives a uniform

coating layer without defects **(Fig. S2, ESI†)**. Finally, the HPI membranes were converted to TR-PBOI membranes after thermal rearrangement at 400 ^{o}C for 2 hr in a furnace under an Ar atmosphere, yielding TR-NFM and TR-NCM membranes. The thermal rearrangement procedure was optimized to obtain 100% conversion from HPI to TR-PBOI (**Section S6, ESI†**), and the extent of conversion was quantified using thermal gravimetric analysis (TGA, Q-500, TA, USA) and attenuated total reflection infrared spectroscopy (ATR-IR, Nicolet 6700, Thermo, USA) in **Fig. S3, ESI†**. Since the membrane thickness critically affected the overall performance,[30] the membranes were fabricated with the same thickness.

All of the TR membranes were successfully fabricated and their morphology, roughness, hydrophobicity, pore size distribution, porosity, LEP, and thermal conductivity were characterized, as summarized in **Fig. 2** and **Table 1**. A commercial GVHP membrane (PVDF, Millipore, Germany), which is widely used as a comparison membrane in literature[10], was also employed in this study. The SEM, AFM and contact angle data of GVHP are summarized in **Fig. S4, ESI†**.

Several distinct trends can be deduced from the characterization data. First of all, the TR-NFM-1 and TR-NFM-2 nanofibers were fused together after thermal rearrangement, resulting in an enhancement in the mechanical strengths of the membranes[27] and a decrease in the voids within the membranes that could induce the adverse wetting phenomena.[31] The distance between the nanofibers became narrower during thermal rearrangement from HPI to PBOI (**Fig. S4e-f, ESI†**). In addition, the advantage of using TR-PBOI particles over inorganic particles is

clearly illustrated as the TR-PBOI particles fused together with the TR-PBOI support during the thermal rearrangement process, preventing particle detachment from the support. Second, although the hot-pressing step can improve the LEP, the contact angle and porosity of TR-NFM-2 were significantly lower than those of TR-NFM-1 because the hot-pressing step reduced the surface roughness of the TR-NFM-2 membrane. Third, the LEP of the hot-pressed membrane (TR-NFM-2) and the surface coated membranes (TR-NCMs) doubled compared to that of the nascent membrane (TR-NFM-1). As expected, the pore size, porosity, and hydrophobicity of the hot pressed membrane (TR-NFM-2) decreased, whereas the surface coated nanocomposite membranes (TR-NCMs) maintained their initial values with slight decreases in pore size. Finally, the pore size distributions of TR-NCMs also became narrower as shown in **Fig. S5, ESI†**. TR-NCM-2 (0.32 ± 0.177 μm, ε = 83 ± 3.4 %) had a slightly larger pore size than TR-NCM-1 (0.27 ± 0.158 μm, ε = 78 ± 2.4 %) with a porosity similar to that of TR-NFM-1 (ε = 81 ± 1.4 %). This is because the sea-squirt shaped TR particles of TR-NCM-2 have a porous morphology with larger particle sizes (*ca.* 1.2 μm) compared to the rigid sphere shaped TR particles (TR-NCM-1, *ca.* 0.55 μm).

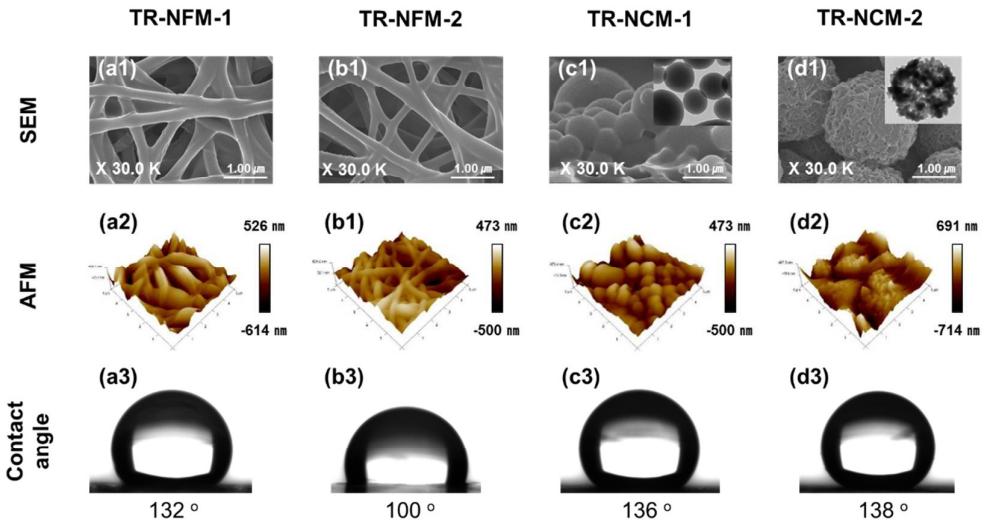

Fig. 2 Surface characterization of TR-PBOI nanofibrous (NFM) and nanocomposite (NCM) membranes. FE-SEM, AFM and deionized (D.I.) water contact angle images of NFM-1 (a1-3), NFM-2 (b1-3), NCM-1 (c1-3) and NCM-2 (d1-3). TEM images (c1 and d2) of TR particles for NCM-1 and NCM-2 are within the SEM images (c1 and d1), respectively.

Table 1 Characterization of TR-PBOI membranes and commercial PVDF membrane.

Samples	Thickness (μm)	Contact angle (°)	Roughness (nm)	Pore size (μm)	Porosity (%)	LEP_w (bar)	Thermal conductivity [2] (W m^{-1} K^{-1})	$\Delta G^*_{het}/\Delta G^*_{hom}$ [3]
GVHP [1]	125 ± 0.4	120 ± 0.2	146 ± 32.2	0.19 ± 0.116	75 ± 1.6	2.4 ± 0.08	0.069 ± 0.0028	0.82 ± 0.002
TR-NFM-1	60 ± 1.2	132 ± 3.7	101 ± 17.6	0.38 ± 0.214	81 ± 1.4	0.5 ± 0.05	0.070 ± 0.0024	0.88 ± 0.010
TR-NFM-2	60 ± 1.7	100 ± 3.3	69 ± 14.6	0.21 ± 0.167	64 ± 1.4	1.1 ± 0.08	0.122 ± 0.0025	0.65 ± 0.017
TR-NCM-1	60 ± 1.4	136 ± 2.4	130 ± 34.1	0.27 ± 0.158	78 ± 2.4	1.0 ± 0.12	0.077 ± 0.0042	0.94 ± 0.015
TR-NCM-2	60 ± 1.5	138 ± 1.4	133 ± 38.2	0.32 ± 0.177	83 ± 3.4	1.0 ± 0.05	0.069± 0.0059	0.96 ± 0.008

[1] PVDF commercial membrane was purchased from Millipore® (Germany).
[2] Thermal conductivity was calculated by **eqn (1)**. Thermal conductivity of the PBO dense membrane was measured using a laser flash method: thru-plane (ASTM E1461).
[3] The energy ratio of heterogeneous and homogeneous nucleation was calculated by **eqn (2).**

The thermal conductivities of the membranes, calculated using **eqn (1)**, changed dramatically with the membrane porosity.[32]

$$k_m = k_a \times \varepsilon + k_p \times (1 - \varepsilon) \quad \textbf{(1)}$$

where k_m, k_p and k_a are thermal conductivities of the membrane, polymer and the air, respectively; ε is the porosity of the membrane.

To minimize heat loss and maximize heat efficiency, a low thermal conductivity is preferred for MD applications. Although the thermal conductivity of the dense TR-PBOI film (0.258 W m^{-1} K^{-1}) is slightly higher than that of the PVDF dense film (0.20 W m^{-1} K^{-1}), it can be seen in **Table 1** that the thermal conductivities of the porous PVDF (GVHP, 0.069 W m^{-1} K^{-1}) and TR-PBOI nanofibrous membrane (TR-NFM-1, 0.070 W m^{-1} K^{-1}) were quite similar when the porosity was taken into account. Since the air has a much lower thermal conductivity (0.0257 W m^{-1} K^{-1}) compared to the polymer, the overall thermal conductivity decreases significantly with increasing porosity. Along the same logic, the thermal conductivity of TR-NFM-2 (ε = 64 %) is much higher compared to other membranes due to its relatively lower porosity.

The prepared membranes were tested in the direct contact membrane distillation (DCMD) configuration (**Section S8, ESI†**). A rectangular Teflon cell with an effective area of 0.00181 m^2 was used as shown in **Fig. S6, ESI†**. A balance that collects the permeate automatically recorded the mass data at 10 min

intervals. The conductivities of feed (synthetic sea water, 0.5 M NaCl aqueous solution) and permeate (D.I. water) were recorded every 10 minutes to synchronize with the mass balance measurements.

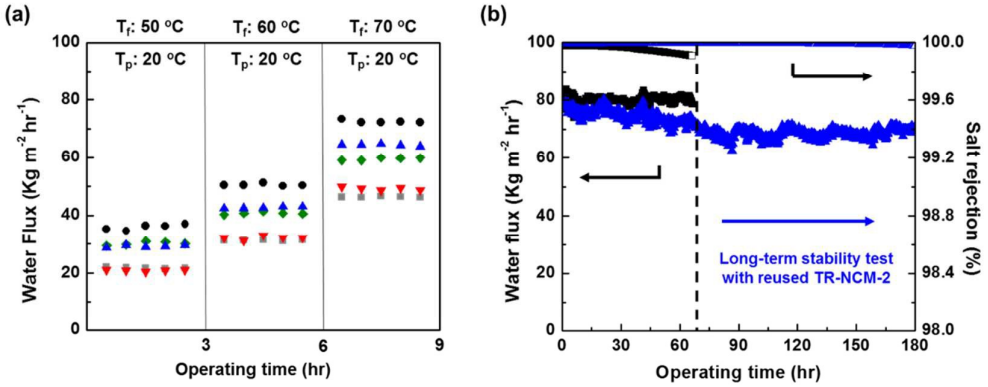

Fig. 3 DCMD tests of GVHP (■), TR-NFM-1 (●), TR-NFM-2 (▼), TR-NCM-1 (♦) and TR-NCM-2 (▲) were measured (a) at different feed temperatures (50, 60 and 70 °C) with 1.0 L min^{-1} flow rates using synthetic sea water (0.5 M NaCl aqueous solution) as a feed solution and D.I. water as a permeate solution at 20 °C. (b) Long-term stability test of TR-NFM-1 (●) and TR-NCM-2 (▲) was conducted using synthetic sea water (0.5 M NaCl aqueous solution) as a feed (70 °C) and D.I. water as a permeate (20 °C) with 2 L min^{-1} of flow rates for more than 66 hr, after then TR-NCM-2 was washed and retested for 120 hr.

The prepared membranes were tested in a range of feed temperatures as shown in **Fig. 3a**. It can be seen that the water flux for all the membranes increase with feed temperature as the vapor pressure (driving force) is exponentially proportional to the feed temperature.[1, 4] In addition, the observed water flux generally increased in accordance with the membrane pore size (**Fig. S5, ESI**†). As expected, TR-NFM-1, which has the largest pore size, exhibited the highest water flux (72 Kg m^{-2} hr^{-1}) at 70 °C and 1.0 L min^{-1} feed flowrate. The tested

membranes exhibited excellent salt rejection (> 99.99 %) during the test as shown in **Fig. S7 (ESI†)**.

The particle coating caused the flux to decrease slightly due to the shadow effect[8, 10, 33] as shown in **Fig. S8, ESI†**. Hence, although the particle coating certainly prevents the membrane from wetting, the shadow effect of the particles increased the mass transfer resistance. The particle coating layer of TR-NCM-1 was densely coated with small dense particles (0.55 μm) compared with that of TR-NCM-2 (porous sea-squirt particle size: 1.2 μm). Therefore, the mass transfer resistance of TR-NCM-1 was higher than those of TR-NCM-2 and TR-NFM-1. Consequently, the water flux of TR-NCM-1 was lower than those of TR-NCM-2 and TR-NFM-1.

The porosity (75 %), contact angle (120 ^{o}) and roughness (146 nm) of GVHP were higher than those (64 %, 100 ^{o} and 69 nm) of TR-NFM-2. Hence, it can be deduced that GVHP membrane would have broader transfer channel for the water vapor, higher water curvature on the surface pores for evaporation of the water vapor, and lower temperature polarization (TP) from the induced turbulent flow compared to those of TR-NFM-2. On the other hand, the larger thickness (125 μm) and lower surface porosity (28.7 %, shown in **Fig. S9, ESI†**) of GVHP reduced the water vapor transport through the membrane and diminished the effective area for the water vapor to evaporate than those (60 μm and 38.9 %) of TR-NFM-2, respectively (**Fig. S9, ESI†**). In particular, the two-fold larger thickness of GVHP compared to TR-NFM-2 significantly affected the water flux of GVHP because

the membrane thickness is exponentially proportional to the mass transfer resistance.[34] Therefore, the water flux of GVHP and TR-NFM-2 seemed to be similar at low flow rate as the merits were offset by their demerits.

Although large pore size is preferred for high water flux, it can also lower the LEP in a membrane. Considering that the TR-NFM-1 has a low LEP (0.5 bar), the operating pressure was limited to 0.3 bar (when the flow rates of feed and permeate are 2.0 L min^{-1}). Since high flow rates can effectively mix the bulk and membrane surface solutions to reduce the thickness of the thermal boundary layer and to increase thermal gradient,[8, 35, 36] the reduced temperature polarization at high flow rate could increase the vapor pressure difference and, consequently, enhance the water flux of the membrane. As expected, the water flux of the prepared membranes also exhibited the same dependency on the flow rate (**Fig. S10, ESI†**). Therefore, a reasonable balance between the membrane properties and flow rate needs to be considered for optimal MD performance as well as operating cost. Among the prepared membranes, TR-NFM-1 and TR-NCM-2 exhibited outstanding performance, and hence they were tested for long-term stability at 2.0 L min^{-1}.

As shown in **Fig. 3b**, both TR-NFM-1 and TR-NCM-2 showed outstanding and stable performance as well as high water flux for more than 66 hr. Again, TR-NFM-1 showed a slightly higher water flux (79.2 kg m^{-2} hr^{-1}) than TR-NCM-2 (77.9 kg m^{-2} h^{-1}) at 2.0 L min^{-1} of flow rate. However, a slow decay of salt rejection for TR-NFM-1 is clearly visible, resulting from liquid water penetration

through the membrane pores. On the other hand, the salt rejection for TR-NCM-2 stayed constant over the same time span, confirming our initial hypothesis that surface coating of the porous nanofibrous membranes improves the LEP and the long-term stability without significant reduction in water flux. After the long-term test, the cross-sections of TR-NCMs observed by SEM confirmed that TR-PBOI particles were still securely fused to the nanofibers as shown in **Fig. S11, ESI†**.

The long-term stability of TR-NCM-2 was further tested for 120 hrs more after cleaning the DCMD apparatus. As shown in **Fig. 3b**, the water flux and salt rejection of TR-NCM-2 were steady during the extended long-term test. In addition, the excellent chemical stability of pristine TR-PBOI membrane (TR-NFM-1) in organic solvents, acid and base solutions (NMP, DMAc, DMSO, H_2SO_4 and 3 M KOH_{aq}) were tested to verify that the TR-PBOI membranes could intrinsically withstand harsh chemical cleaning conditions (**Fig. S12, ESI†**).

Furthermore, the potential of TR-PBOI membranes for MCr was investigated using highly concentrated feed solutions (1, 3 and 5 M of NaCl aqueous solution), as shown in **Fig. S13, ESI†**. Although the water flux of TR-NFM-1 decreased in accordance with the increasing feed concentration due to the colligative property, the salt rejection of TR-NFM-1 remained above 99.99 % at all temperatures and concentrations of the feed solution during the test.

Based on this result, TR-NFM-1 was initially tested using the MCr configuration (**Section S9, ESI†**). It was observed that, after 3 h of operation, the

size of the produced NaCl crystals was 123 ± 22 μm and the crystal size was a function of operating time (**Fig. S14, ESI†**). In MCr, the crystal formation on the surface of the membrane is induced by heterogeneous nucleation, which generally requires less energy relative to the homogeneous nucleation in a pure saturated solution.[19, 23] Solute molecules can reach local supersaturation conditions in the surface pores where heterogeneous nucleation can occur with lower energy. The energy difference between the heterogeneous and homogeneous nucleation can be described using the following equation.[22, 23]

$$\frac{\Delta G^*_{het}}{\Delta G^*_{hom}} = \frac{1}{4}(2+\cos\alpha)(1-\cos\alpha)^2\left[1-\varepsilon\frac{(1+\cos\alpha)^2}{(1-\cos\alpha)^2}\right]^3 \quad \textbf{(2)}$$

where α is the surface contact angle with the crystallizing solution and ε is the porosity of the membrane.

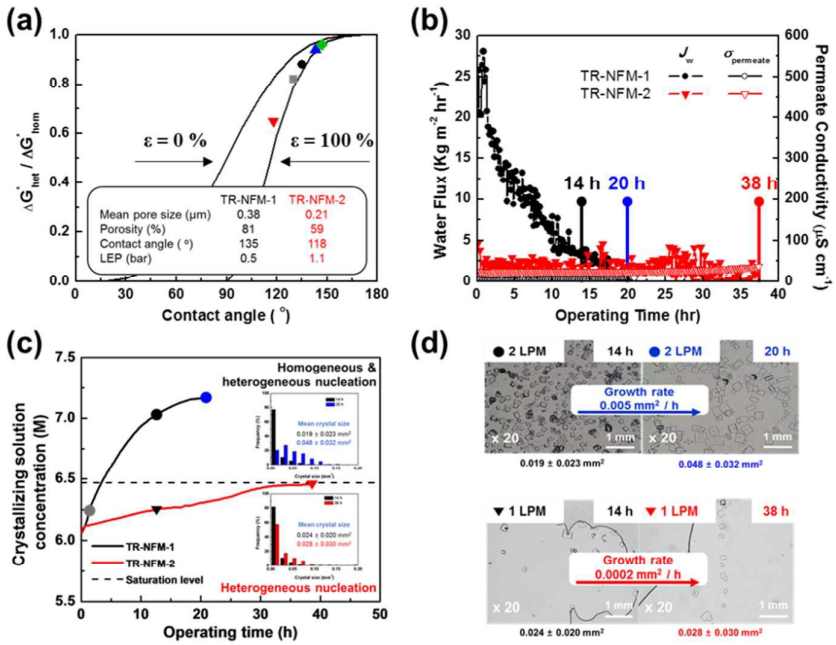

Fig. 4 (a) $\Delta G^{*}_{het}/\Delta G^{*}_{hom}$ ratio of GVHP (■), TR-NFM-1 (●), TR-NFM-2 (▼), TR-NCM-1 (▲) and TR-NCM-2 (♦) were calculated using **eqn. (2)**. (b) The water flux and permeate conductivity were measured with TR-NFM-1 and TR-NFM-2 using 352.6 g L^{-1} NaCl aqueous solution and D.I. water as the feed (50 ^{o}C) and permeate (20 ^{o}C) solutions with 2 and 1 L min^{-1} flow rates, respectively. (c) Concentration profiles of the crystallizing solution during the MCr operation: TR-NFM-1 (–), TR-NFM-2 (–) and saturated concentration of NaCl aqueous solution at 50 ^{o}C (--). The crystal size distributions of the produced NaCl crystal were analyzed using an aliquot sample after 2 hr (●), 14 hr (●), 20 hr (●), 14 hr (▼) and 38 hr (▼) of operation for TR-NFM-1 and TR-NFM-2. (d) Optical microscopy images of the crystals were analyzed using the ImageJ program. The saturation concentration of NaCl aqueous solution at 50 ^{o}C is 6.47 M.

As illustrated in **Fig. 4a**, **eqn (2)** predicts that heterogeneous nucleation is favored with lower contact angle and higher porosity. Therefore, in terms of long-term stability, TR-NFM-1 exhibited slightly higher tendency for salt crystallization in the surface of TR-NFM-1 membrane than that of TR-NCM-2 membrane. TR-NFM-2, with the lowest contact angle, exhibited the lowest energy requirement for heterogeneous nucleation compared to the other tested membranes. However, note that lower contact angle induces a detrimental wetting phenomenon, which should be avoided. In addition, crystal growth rate in the MCr is also affected by the process parameters such as water flux and feed flow rate.[22, 23] Therefore, to investigate the influence of nucleation energy ratio and process parameters on MCr performance, TR-NFM-1 and TR-NFM-2 were tested in the MCr configuration.

The water flux and permeate conductivity of TR-NFM-1 and TR-NFM-2 are shown in **Fig. 4b**. In contrast to the MD experiment, TR-NFM-1 showed a rapid decline in water flux. This is a common phenomenon in MCr processes with large

pore size membranes, resulting from pore wetting by salt crystallization.[18, 19, 23] On the other hand, TR-NFM-2 maintained steady flux and stable rejection throughout the 38 hr operation. NaCl crystals made using TR-NFM-2 (▼, 0.024 ± 0.020 mm^2) showed larger crystal sizes with narrower crystal distributions than those of TR-NFM-1 (●, 0.019 ± 0.023 mm^2) after 14 hr of operation, as shown in **Fig. 4c** and **4d**.

As G^*_{het}/G^*_{hom} of TR-NFM-2 is lower than that of TR-NFM-1, more heterogeneous nucleation was expected for TR-NFM-2 membranes. In the case of TR-NFM-1, NaCl crystals were observed only when the crystallizing solution reached the saturation concentration (6.45 M at 50 ^oC), as shown in **Fig. S15, ESI†**. After 14 hr, the crystallizing solution concentration (7.06 M) was already above the saturation level due to the high flux, indicating that most of the nucleation occurred via homogeneous nucleation (**Fig. 4c**).

On the other hand, for TR-NFM-2 membranes, NaCl crystals were clearly visible below the saturation point (**Fig. 4c**), indicating that all of the nucleation was induced by heterogeneous nucleation. However, TR-NFM-1 clearly shows more crystal generation and faster crystal growth (0.005 mm^2 hr^{-1}) compared to the TR-NFM-2 membrane (0.0002 mm^2 hr^{-1}), mainly due to the difference in water flux. In addition, it was observed that 2 L min^{-1} flow rate (0.019 ± 0.023 mm^2) produced larger crystals with broader crystal distribution than those of 1 L

min^{-1} (0.017 ± 0.011 mm^2) after 14 hr of operation with TR-NFM-1 (**Fig. S16, ESI†)**.

This suggests that the membranes can certainly induce heterogeneous nucleation, but other parameters such as flow rates and water flux significantly affect the crystal formation and growth kinetics. Hence, in order to fully exploit the heterogeneous nucleation of MCr, the process flow rate and flux must also be controlled.

TR-NFM-1 was also tested with a 184.6 $g.L^{-1}$ Na_2SO_4 aqueous solution as the feed (50 ^oC) and D.I. water as permeate (20 ^oC). As shown in **Fig. S17, ESI†**, the divalent crystal system showed longer flux stability and larger crystals compared to the monovalent (NaCl) MCr data. It was also observed that the crystal formation rate significantly increased with the flow rate. Hence, prepared electrospun TR-PBOI membranes show promising potential for MCr, especially for large crystals such as epsomite ($MgSO_4 \cdot 7H_2O$) and proteins. A detailed investigation comparing the membranes with different surface roughness and morphology on the crystal formation kinetics will be the subject of our upcoming publications.

Conclusion

In summary, thermally rearranged polybenzoxazole-co-imide (TR-PBOI) nanofibrous membranes were successfully fabricated using electrospun HPI nanofiber as a precursor. To improve the LEP of the nanofibrous membranes, two different types of TR-PBOI particles were fabricated and then coated onto the membrane surface. The fabricated membranes showed excellent performance and ideal characteristics such as high hydrophobicity and high porosity. When tested in MD, TR-NFM-1 and TR-NCM-2 exhibited stable performance with high water flux as well as excellent salt rejection. Thermal treatment of the precursor membranes resulted in well-connected structures between the fibers and the particles, preventing particle detachment from the nanofibrous support. In addition, the TR-PBOI particles improved the surface roughness and plugged the large surface pores of TR-NFM-1, increasing the LEP and promoting heterogeneous nucleation while narrowing the pore size distribution without decreasing the membrane porosity. The surface coated TR-NCM-2 membranes exhibited excellent long-term stability compared to the nascent TR-NFM-1, overcoming the key challenge of nanofibrous membranes. Furthermore, the heterogeneous nucleation phenomena were controlled using the morphology of TR membranes, suggesting that the membranes can also be applied for membrane crystallization processes.

Electronic supplementary information available

Detailed experimental methods and characterizations were described in the ESI†.

Acknowledgements

We appreciate the financial support from the Nano Material Technology Development Program (2012M3A7B4049745) through the National Research Foundation (NRF) funded by the Ministry of Science, ICT and Future Planning.

References

1. E. Curcio and E. Drioli, *Sep. Purif. Rev.*, 2005, **34**, 35-86.
2. M. S. El-Bourawi, Z. Ding, R. Ma and M. Khayet, *J. Membr. Sci*, 2006, **285**, 4-29.
3. M. Khayet, *Adv. Colloid Interface Sci.*, 2011, **164**, 56-88.
4. L. D. Tijing, J.-S. Choi, S. Lee, S.-H. Kim and H. K. Shon, *J. Membr. Sci.*, 2014, **453**, 435-462.
5. V. Thavasi, G. Singh and S. Ramakrishna, *Energy Environ. Sci.*, 2008, **1**, 205.
6. D. Cohen-Tanugi, R. K. McGovern, S. H. Dave, J. H. Lienhard and J. C. Grossman, *Energy Environ. Sci.*, 2014, **7**, 1134-1141.
7. A. ElMekawy, H. M. Hegab and D. Pant, *Energy Environ. Sci.*, 2014, **7**, 3921-3933.
8. A. Razmjou, E. Arifin, G. Dong, J. Mansouri and V. Chen, *J. Membr. Sci.*, 2012, **415-416**, 850-863.
9. H. Maab, L. Francis, A. Al-saadi, C. Aubry, N. Ghaffour, G. Amy and S. P. Nunes, *J. Membr. Sci*, 2012, **423-424**, 11-19.
10. Y. Liao, R. Wang and A. G. Fane, *Environ. Sci. Technol.*, 2014, **48**, 6335-6341.
11. X. Li, C. Wang, Y. Yang, X. Wang, M. Zhu and B. S. Hsiao, *ACS Appl. Mater. Inter.*, 2014, **6**, 2423-2430.
12. F. Guo, A. Servi, A. Liu, K. K. Gleason and G. C. Rutledge, *ACS Appl. Mater. Inter.*, 2015, **7**, 8225-8232.
13. C. Yang, X.-M. Li, J. Gilron, D.-f. Kong, Y. Yin, Y. Oren, C. Linder and T. He, *J. Membr. Sci*, 2014, **456**, 155-161.
14. S. Cavaliere, S. Subianto, I. Savych, D. J. Jones and J. Rozière, *Energy Environ. Sci.*, 2011, **4**, 4761.

15. H. Gwon, J. Hong, H. Kim, D.-H. Seo, S. Jeon and K. Kang, *Energy Environ. Sci.*, 2014, **7**, 538-551.
16. G. Zhou, F. Li and H.-M. Cheng, *Energy Environ. Sci.*, 2014, **7**, 1307-1338.
17. J. F. Kim, J. H. Kim, Y. M. Lee and E. Drioli, *AIChE Journal*, 2015, n/a-n/a.
18. E. Curcio, A. Criscuoli and E. Drioli, *Ind. Eng. Chem. Res.*, 2001, **40**, 2679-2684.
19. E. Drioli, G. Di Profio and E. Curcio, *Curr. Opin. in Chem. Eng.*, 2012, **1**, 178-182.
20. B. Van der Bruggen, *Ind. Eng. Chem. Res.*, 2013, **52**, 10335-10341.
21. G. D. Profio, M. Polino, F. P. Nicoletta, B. D. Belviso, R. Caliandro, E. Fontananova, G. D. Filpo, E. Curcio and E. Drioli, *Adv. Funct. Mater.*, 2014, **24**, 1582-1590.
22. E. Curcio, E. Fontananova, G. Di Profio and E. Drioli, *J. Phys. Chem. B*, 2006, **110**, 12438-12445.
23. G. Di Profio, E. Curcio and E. Drioli, *Ind. Eng. Chem. Res.*, 2010, **49**, 11878-11889.
24. H. B. Park, C. H. Jung, Y. M. Lee, A. J. Hill, S. J. Pas, S. T. Mudie, E. Van Wagner, B. D. Freeman and D. J. Cookson, *Science*, 2007, **318**, 254-258.
25. K. T. Woo, J. Lee, G. Dong, J. S. Kim, Y. S. Do, W.-S. Hung, K.-R. Lee, G. Barbieri, E. Drioli and Y. M. Lee, *J. Membr. Sci.*, 2015, **490**, 129-138.
26. S. H. Han, N. Misdan, S. Kim, C. M. Doherty, A. J. Hill and Y. M. Lee, *Macromolecules*, 2010, **43**, 7657-7667.
27. M. J. Lee, J. H. Kim, H. S. Lim, S. Y. Lee, H. K. Yu, J. H. Kim, J. S. Lee, Y. K. Sun, M. D. Guiver, K. D. Suh and Y. M. Lee, *Chem. Commun.*, 2015, **51**, 2068-2071.
28. A. Pongpeerapat, C. Wanawongthai, Y. Tozuka, K. Moribe and K. Yamamoto, *Int. J. Pharm.*, 2008, **352**, 309-316.
29. L. Wu, J. Zhang and W. Watanabe, *Adv. Drug. Deliv. Rev.*, 2011, **63**, 456-469.
30. H. Y. Wu, R. Wang and R. W. Field, *J. Membr. Sci.*, 2014, **470**, 257-265.
31. Y. Liao, R. Wang, M. Tian, C. Qiu and A. G. Fane, *J. Membr. Sci.*, 2013, **425-426**, 30-39.
32. A. Boubakri, R. Bouchrit, A. Hafiane and S. A. Bouguecha, *Environ. Sci. Pollut. Res.*, 2014, **21**, 10493-10501.
33. Y. Liao, R. Wang and A. G. Fane, *J. Membr. Sci*, 2013, **440**, 77-87.
34. M. Essalhi and M. Khayet, *J. Membr. Sci.*, 2014, **454**, 133-143.
35. F. Laganà, G. Barbieri and E. Drioli, *J. Membr. Sci*, 2000, **166**, 1-11.
36. T. Y. Cath, V. D. Adams and A. E. Childress, *J. Membr. Sci*, 2004, **228**, 5-16.

Graphical abstract

Thermally Rearranged Polymer Membranes for Desalination

Ji Hoon Kim[1], Sang Hyun Park[1], Moon Joo Lee[2],

Sang Min Lee[1], Won Hyo Lee[1], Kang Hyuck Lee[1],

Na Rae Kang[1], Hye Jin Jo[1], Jeong F. Kim[1],

Enrico Drioli[1, 3, *] and Young Moo Lee[1, 2, *]

[1]Department of Energy Engineering, College of Engineering, Hanyang University, Seoul 133-791, Republic of Korea

[2]Division of Chemical Engineering, College of Engineering, Hanyang University, Seoul 133-791, Republic of Korea

[3]Institute on Membrane Technology (ITM-CNR), University of Calabria, Rende, Cosenza, Italy

***Corresponding authors:**

Y. M. Lee (ymlee@hanyang.ac.kr),

E. Drioli (e.drioli@itm.cnr.it)

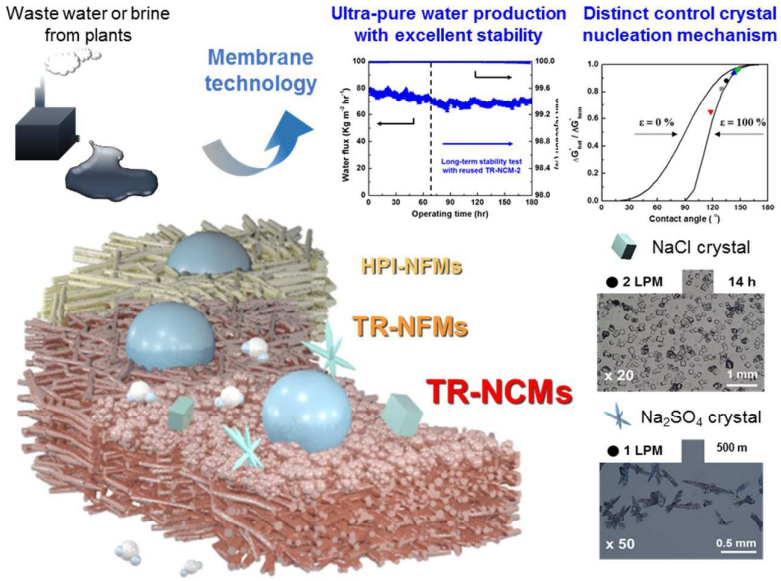

Thermally rearranged polybenzoxazole-co-imide (TR-PBOI) nanofibrous and nanocomposite membranes (NFM and NCM) were developed for membrane distillation and membrane crystallization applications. The TR-PBOI membranes exhibited excellent flux (80 kg m^2 hr^{-1}) and salt rejection (> 99.99 %) over more than 186 hours. These membrane also showed potential for use in membrane crystallization.

Electronic Supplementary Information

Thermally Rearranged Polymer Membranes for Desalination

Ji Hoon Kim[1], Sang Hyun Park[1], Moon Joo Lee[2],

Sang Min Lee[1], Won Hyo Lee[1], Kang Hyuck Lee[1],

Na Rae Kang[1], Hye Jin Jo[1], Jeong F. Kim[1],

Enrico Drioli[1, 3, *] and Young Moo Lee[1, 2, *]

[1] Department of Energy Engineering, College of Engineering,

Hanyang University, Seoul 133-791, Republic of Korea

[2]Division of Chemical Engineering, College of Engineering, Hanyang University,

Seoul 133-791, Republic of Korea

[3]Institute on Membrane Technology (ITM-CNR), University of Calabria, Rende,

Cosenza, Italy

***Corresponding authors:**

Y. M. Lee (ymlee@hanyang.ac.kr),

E. Drioli (e.drioli@itm.cnr.it)

0. Background

Most of the developed MD membranes can be fabricated using two types of fabrication methods: phase inversion method and electrospinning method. The phase inversion method is a well-known conventional technique to fabricate asymmetric membranes with variety of morphologies. On the other hand, the electrospinning method can fabricate highly porous, thin and flexible membrane with high porosity.[1] We have summarized the pros & cons of the two fabrication methods for membrane distillation application as shown in **Table S1**.

Table S1 Summary of pros & cons between phase-separation and electrospun membranes for membrane distillation application.

Membrane Distillation Application	Phase-separation Membrane	Electrospun Membrane
Pros	*Stable performance* • High LEP • Narrow pore size distribution	*High water flux* • High porosity • Inter-connected pore structure • Large pore size • Thin, rough surface
Cons	*High mass transport resistance* • Thick • Low porosity • Small pore size	*Poor long-term stability* • Broad pore size distribution • Difficult handling

As shown in **Table S1**, there is a trade-off between the long-term stability and the MD flux. For instance, membranes fabricated using the phase inversion method shows high stability but relatively lower permeability, and membranes fabricated using the electrospinning method shows high permeability but lower long-term stability.

Table S2 summarizes the recent DCMD publication data in the literature. It can be seen that the membranes prepared using the phase inversion method generally shows lower permeability but excellent long-term stability due to their low porosity and high thickness. Notably, one of the reported data showed stability up to 300 hr.[2] On the other hand, many researchers have recently focused on preparing electrospun membranes due to their high water flux and excellent salt rejection. However, not many researchers have reported the long-term stability data.

Table S2 Recently published DCMD data of flat-sheet type membranes in literature.

Material	Type	LEP (bar)	Pore size (μm)	Thickness (μm)	Porosity (%)	Feed (°C)	Permeate (°C)	Water flux (Kg m^{-2} hr^{-1})	Long-term Stability (hr)	Published year	Ref.
PVDF	Phase separation	2.0	0.12	N/A	N/A	3.5 wt% $NaCl_{aq}$ (80)	DI water (17)	14	48	2014	3
PTFE	Millipore commercial	1.5	0.22	175	70	3.5 wt% $NaCl_{aq}$ (80)	DI water (20)	40	70	2014	4
PVDF / fabric	Phase-separation	6	0.22	213	55	3.5 wt% $NaCl_{aq}$ (50)	DI water (20)	13	240	2012	5
PVDF	Phase-separation	8.9	0.33	330	64	3.5 wt% $NaCl_{aq}$ (50)	DI water (17.5)	15	300	2014	2
TRPBOI TR-NCM-2	**Electro-spinning**	**1.0**	**0.28**	**60**	**83**	**0.5 M $NaCl_{aq}$ (70)**	**DI water (17.5)**	**79**	**186 (66 + 120)**	**2015**	**In this study**
SiO_2 nps PVDF	Electro-spinning	1.8	0.68	130	83	3.5 wt% $NaCl_{aq}$ (60)	DI water (20)	18.9	50	2014	6
PS	Electro-spinning	0.8	0.62	120	78	3.5 wt% $NaCl_{aq}$ (70)	DI water (20)	51	10	2014	7
Ag nps PVDF	Electro-spinning	1.5	0.34	47	66	3.5 wt% $NaCl_{aq}$ (60)	DI water (20)	32	8	2013	8
F-PT	Electro-spinning	0.9	2.7	N/A	N/A	3.5 wt% $NaCl_{aq}$ (70)	DI water (20)	61	N/A	2012	9

As can be seen in **Table S2**, the present TR-PBOI membranes exhibited the highest water flux and excellent salt rejection for a long time compared with other reported electrospun membranes. Most of the electrospun membranes reported in

the literature showed significant performance degradation with operation time or did not report any long-term data.

1. Materials

Two kinds of diamines and dianhydride were used for the synthesis of hydroxy polyimide (HPI) as a precursor of thermally rearranged polybenzoxazole-co-imide (TR-PBOI) (**Scheme S1**). 4,4'-oxydiphthalic anhydride (ODPA) was purchased from Shanghai Resin factory Co. Ltd. (Shanghai, China). 3,3'-dihydroxy-4,4'-diamino-biphenyl (HAB) and 4,4'-oxydianiline (ODA) were obtained from Sigma-Aldrich Chemical Co. (Milwaukee, WI, USA). *N*-Methyl-2-pyrrolidone (NMP) and *o*-xylene from Sigma-Aldrich Chemical Co. were used as solvents for the synthesis of polymers, and *N,N*-dimethylacetamide (DMAc), poly(vinyl alcohol) (PVA, Mw of 85,000) and poly(vinyl pyrrolidone) (PVP, Mw of 40,000) were purchased from Sigma-Aldrich Chemical Co. for preparation of nano-fibers and particles.

2. Synthesis of hydroxyl polyimide as a precursor polymer for thermally rearranged polybenzoxazole-co-imide

The procedure for synthesizing hydroxy polyimide is described in **Scheme S1** and in our previous studies.[3, 4] All monomers (ODPA, HAB, and ODA) were dried overnight in a vacuum oven at ambient temperature. Diamines (ODA and HAB, 25 mmol, respectively) were dissolved in a 500 mL four neck round-bottomed flask filled with anhydrous NMP (80 mL) under a nitrogen atmosphere. Once all diamine powders were completely dissolved, the flask was cooled to 0 °C and ODPA monomer (50 mmol) dissolved in NMP (50 mL) was added to initiate polymerization *via* a spontaneous ring opening reaction with diamines. The solution was stirred overnight and a viscous yellowish hydroxyl polyamic acid (HPAA) solution was obtained. To convert HPPA to hydroxy polyimide (HPI) *via* azeotropic imidization, *o*-xylene (60 ml) as an azeotropic agent was poured into the HPAA solution and the flask temperature was maintained between 160 and 180 ^{o}C for 6 hr. After removing the water generated by the imidization reaction, the solutions were precipitated in a water/methanol solution (3:1 ratio) using a mechanical mixer, and they were subsequently dried in a vacuum oven at 150 ^{o}C for 12 hr.

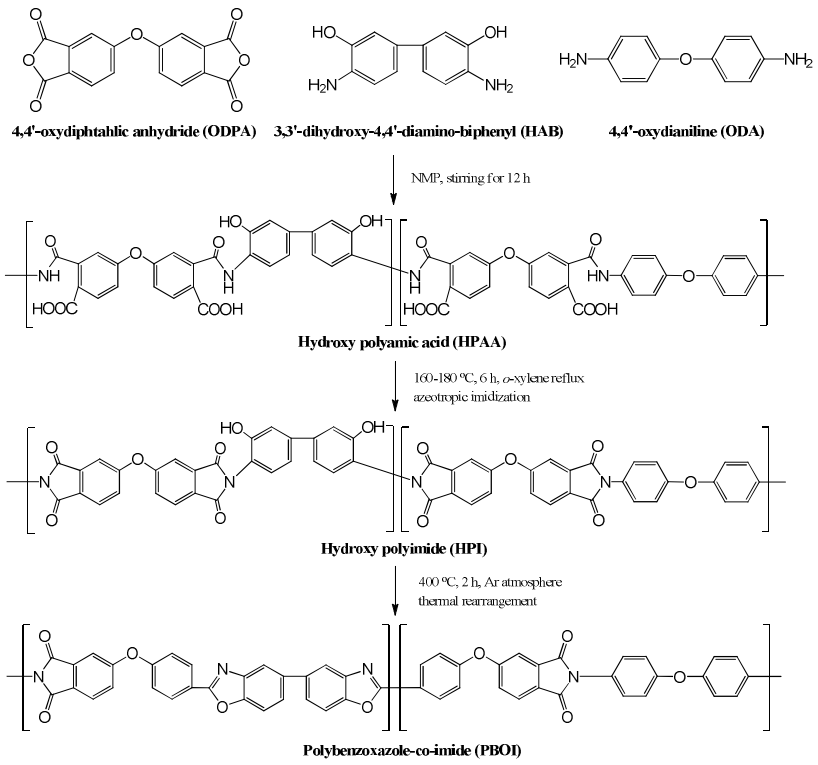

Scheme S1 Synthetic scheme for thermally rearranged polybenzoxazole-co-imide.

3. Electrospinning of HPI polymer

A HPI dope solution was prepared by dissolving the polymer (10 *wt*%) in dimethyl acetamide (DMAc). The HPI solution was stirred overnight at 60 ^{o}C and filtered through an 11 μm nylon filter (Millipore, USA) to prepare a homogenous solution. A multi-nozzle electrospinning apparatus (M-tek, Korea) was purchased, and it consisted of 16 needles (23 gauges) and a drum type collector (total area: 0.0021 m^2). An HPI solution (40 ml) was electrospun onto a collector covered with PET nonwoven fabric with a 15 cm of tip-to-collector distance using a syringe pump (LB-200, Longer Pump, China) set at a flow rate of 4.0 ml h^{-1}. The voltages at the needles and the collector were 28 kV and -4 kV, respectively. During the electrospinning, the needle set traversed along the x-axis rail (25 cm) at 10 mm min^{-1} and the collector rotated at 8 rpm to obtain a uniform HPI nanofibrous membrane. After electrospinning, the HPI membrane was dried at ambient conditions overnight to remove residual solvent. Then, the HPI membrane was carefully detached from the PET nonwoven support, and thermal rearrangement was conducted as described in **Section S6**.

4. Preparation of HPI nanoparticles

HPI particles were prepared by reprecipitation method which is one of the particle formation method using a polymer solution, non-solvent and stabilizer. In this study, initially four different kinds of HPI particles were prepared to investigate effect of two different stabilizers (PVP, Mw 55K and PVA, Mw 90K) on the particle morphology using water as the nonsolvent, as summarized in **Fig. S1** below. HPI polymer was dissolved in NMP with 2 *wt%* of concentration without any stabilizer, and with 2 *wt%* PVP or 2 *wt%* PVA, and 5 *wt%* of concentration with 5 *wt%* PVP. The solutions are designated like HPI2, HPI2PVP2, HPI2PVA2 and HPI5PVP5. All HPI solutions stirred and filtered using 0.5 μm PTFE syringe filter to obtain the homogeneous solutions without impurities. The polymer solution was mechanically stirred with 300 rpm at 70 ^{o}C. Non-solvent added into the polymer solution with 0.05 ml min^{-1} of adding speed using syringe pump. After preparation of HPI particles, the polymer solution was quenched in an ice bath to prevent aggregation of the particles. The particles were filtered and centrifuged to wash off the residual solvent and non-solvent. After freeze drying at 0 ^{o}C for 30 hr or more, the particles were ready to fabricate composite membrane.

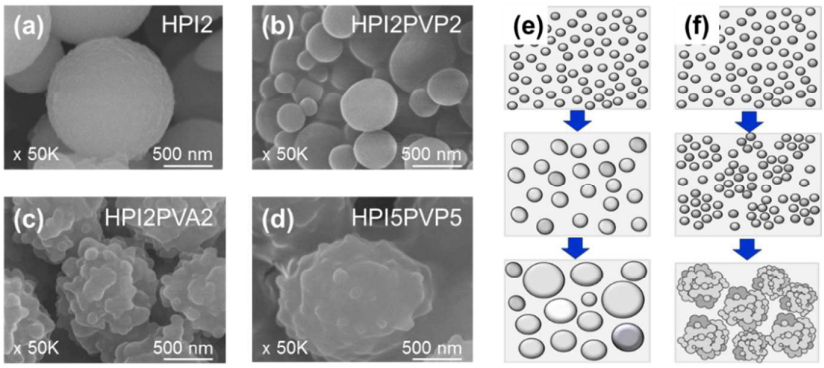

Fig. S1 SEM images of HPI particles in accordance with different stabilizers; (a) without stabilizer, (b) 2 *wt%* of PVP, (c) 2 *wt%* of PVA and (d) 5 *wt%* of PVP. Schematics of suggested particle formation mechanism for (e) spherical and (f) sea-squirt shaped particles.

As shown in **Fig. S1a**, the 2 *wt%* HPI (HPI2) particles which were fabricated without any stabilizer exhibited crumpled morphology without forming discrete particles. The crumpled morphology was formed due to the particle agglomeration in order to minimize the surface energy. Such agglomeration can be prevented using a surfactant stabilizer such as PVP or PVA.[5] It can be seen in **Fig. S1b** that 2 *wt%* PVP additive (PVP2) induced discrete spherical particles with the average diameter of 550 nm. On the other hand, when 2 wt% PVA (PVA2) was used as an additive, the resulting particles exhibited the rough sea-squirt shaped morphology as shown in **Fig. S1c**. Also, the image shows that each particle is made up of many tiny particles fused together. Interestingly, the particles were also porous when examined with TEM (**Fig. 2d1**). Such difference in particle morphology between two additives can be explained using the concept of critical aggregation concentration (CAC), defined as the threshold surfactant concentration at which the interaction between the surfactant and the polymer occurs.[5] **Fig. S1e and S1f** illustrate the particle formation mechanisms for two different additives. Comparing two additives, 2 *wt%* PVP was below the CAC and hence each particle grew in size independently (**Fig. S1e**). On the other hand, 2 *wt%* PVA was above the CAC and hence each particle did not grow in size but formed a secondary particle composed of many primary small particles (**Fig. S1f**). As noted by *Wu et al.* the surfactant acts not only as the stabilizer, but also as the bridge to facilitate agglomeration of primary particles.[6] As shown in **Fig. 2c1 and 2d1**, the porosity of the sea-squirt shaped particles is induced from the boundaries between the small particles. Notably, it can be seen in **Fig. S1d** that the same sea-squirt morphology can also be induced using PVP simply by

increasing the PVP concentration above the CAC.

5. Fabrication of HPI nanocomposite membranes

HPI particles were dispersed into ethanol at a concentration of 1 *wt*%. The solution was sprayed onto the surface of the HPI electrospun membrane using a spray gun (HP-TR 2, Iwata, Japan) with N_2 gas at 0.2 kgf cm^{-2}. The thickness of the coating layer was observed using SEM and the correlation between the coating thickness and the sprayed volume of HPI particles is shown in **Fig. S2**.

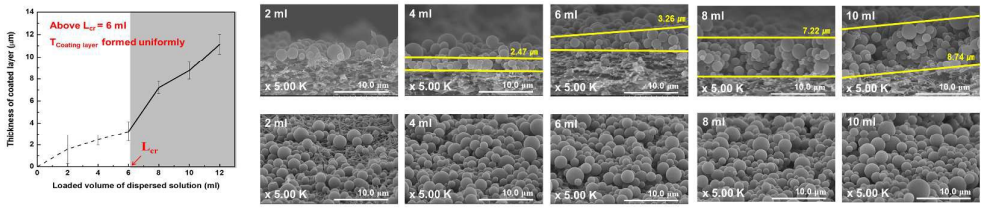

Fig. S2 Thickness of the particle coating layer in accordance with the sprayed volume of the solution with dispersed HPI particles.

The coating layer of HPI particles was uniform and had no defects when > 6 ml solution was sprayed onto the surface. Therefore, we defined a value $L_{cr,}$ which indicates the critical loading amount of a HPI nanoparticle solution for a uniform coating layer and sprayed 8 ml of the solution onto a 0.0088 m^2 area of the HPI nanofibrous membranes. After spray coating, the HPI composite membrane was dried overnight at ambient conditions to remove ethanol.

6. Thermal rearrangement of HPI membranes

The HPI nanofibrous and nanocomposite membranes were converted to TR-PBOI membranes *via* thermal rearrangement in a furnace at 400 ^{o}C under an Ar atmosphere. The furnace was first heated to 300 ^{o}C at 10 ^{o}C min^{-1} and equilibrated at 300 ^{o}C for 1 hr to remove residual solvent and confirm the azeotropic imidization. Then, the furnace was further heated to 400 ^{o}C at 10 ^{o}C min^{-1} and equilibrated for 2 hr for thermal rearrangement.

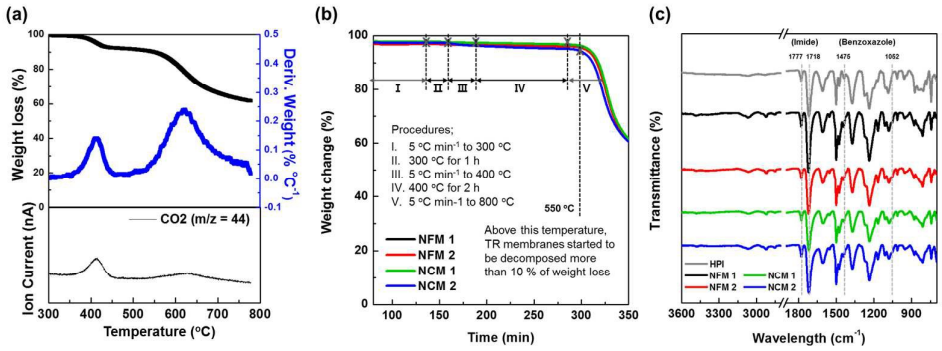

Fig. S3 (a) Thermogravimetric analysis (TGA) and differential thermogram (DTG) curves of HPI nanofibrous membrane with mass spectroscopy of CO_2 on the bottom of the TGA curve. (b) TGA curves and (c) attenuated transmittance reflection infrared (ATR-IR) spectroscopy analysis of TR-PBOI membranes compared with HPI precursor to confirm the thermal stability and thermal rearrangement.

To confirm the thermal rearrangement of the TR-PBOI membranes, thermogravimetric analysis – mass spectroscopy (TGA-mass) and attenuated total reflectance-infrared (ATR-IR) analysis were used for HPI and TR-PBOI membranes. TGA-mass (TA Q-50, TA Instruments, USA and ThermoStar™ GSD 301T, Pfeiffer Vacuum GmbH, Germany) was employed to obtain 100 % TR conversion of the HPI nanofibrous membrane and also to investigate the thermal stability of the TR-PBOI membranes. The HPI membrane was heated up to 800 ^{o}C at 10 ^{o}C min^{-1} in a TGA furnace under a nitrogen atmosphere to observe the weight loss of the

membrane during thermal rearrangement. As shown in **Fig. S3a**, the TGA curve of the HPI membrane showed a weight loss and a CO_2 emission peak in the mass spectroscopy data around 400 ^{o}C. The curve of the differential thermogram (DTG) also exhibited that the thermal rearrangement rate was the highest at 400 ^{o}C. To confirm the thermal rearrangement of all TR-PBOI membranes, each membrane was heated up to 300 ^{o}C at 10 ^{o}C min^{-1} and was equilibrated for 1 hr. After that, the membrane was continuously heated to 400 ^{o}C at 10 ^{o}C min^{-1} and was equilibrated for 2 hr before finally being heated up to 800 ^{o}C at 10 ^{o}C min^{-1} using the TGA. In **Fig. S3b**, All TR-PBOI membranes exhibited excellent thermal stability below 550 ^{o}C without significant weight loss, which suggests that the HPI membranes were completely converted to TR-PBOI membranes. In **Fig. S3c**, the evidence of the conversion from HPI to TR-PBOI can also be observed at 1052 and 1475 cm^{-1}, corresponding to the benzoxazole band, using ATR-IR (Nicolet 6700, Thermo Scientific, MA, USA).

7. Characterization

The surface morphologies of the TR-PBOI membranes were verified with field emission scanning electron microscopy (FE-SEM, Hitachi S-4800, Tokyo, Japan), transmission electron microscopy (TEM, JEOL JEM-2000EXII, Tokyo, Japan) and atomic force microscopy consisting of a digital instruments Multimode 8 (Veeco, NY, USA) and diNanoScope V controller (Veeco). Before the characterization, the membranes were dried in a vacuum oven overnight at 70 ^{o}C to remove residual solvent. The samples for SEM analysis were coated with platinum for 30 s using platinum sputtering (Hitachi E-1045, Tokyo, Japan) and were observed at 15 kV and 10 mA in the SEM chamber under vacuum conditions. For TEM, the samples were embedded in epoxy resin and microtomed using a RMC MTX Ultra microtome (RMC Products, Tucson, AZ, USA). The TEM images were obtained at accelerating voltages of 120 kV. The membranes were also investigated using AFM tapping mode with a silicon probe (Nanosensors, Switzerland) with a force constant of 1.2 – 20 N m^{-1}. The surface roughness was measured using the Nanoscope 8.10 program, and each sample was measured at three different surface regions. The morphologies of TR-PBOI membranes were summarized in **Fig. 2**, and the morphologies of GVHP as a reference membrane (a porous PVDF membrane purchased from Millipore, USA) are summarized in **Fig. S4** together with the cross section SEM images of HPI and TR-PBOI membranes. The hydrophobicity of the membranes were measured using a contact angle analyzer (Phoenix 300, S.E.O, Ansung, Korea) by placing a droplet of deionized water on the membranes and comparing pictures taken 0.5 s after the droplet had fallen. The contact angles of TR-PBOI membranes are displayed in **Fig. 2** and that of the GVHP membrane is provided in **Fig. S4d**.

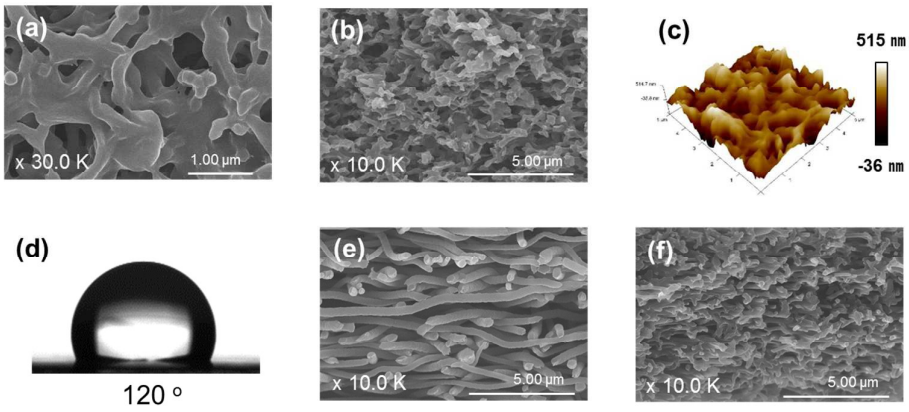

Fig. S4 SEM images of (a) surface and (b) cross section, (c) AFM and (d) contact angle of GVHP membranes. The cross-section SEM images of (e) HPI-NFM-1 and (f) TR-NFM-1.

The mean pore size and pore size distribution of all membranes were investigated using a capillary flow porometer (CFP, 1500AE, Porous Materials, USA) as shown in **Fig. S5**. The samples were immersed in a Galwick solution (surface tension: 15.9 dyne cm^{-1}) for 10 min and were measured using the wet up / dry up method from 0 to 400 psia using N_2 gas.

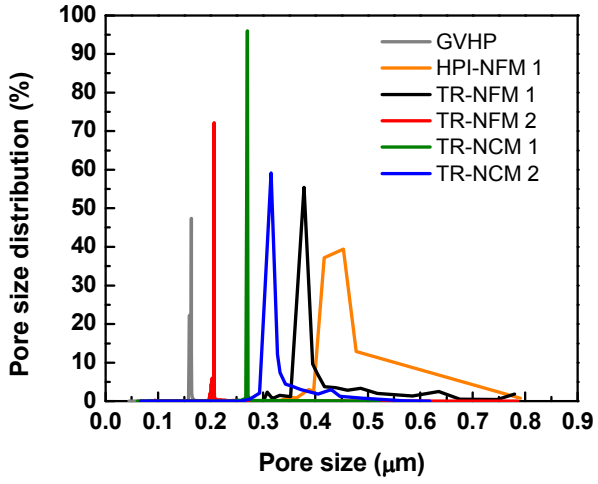

Fig. S5 The pore size distribution of GVHP, HPI-NFM-1, TR-NFM-1, TR-NFM-2, TR-NCM-1 and TR-NCM-2.

The porosity of the membranes was evaluated using n-hexadecane (Alfa Aesar, MA, USA). The samples were prepared at least 5 times for each membrane and the dried and soaked weights of the membranes were recorded. Excess solvent on the surface of the membranes was wiped off before measuring the weight of the soaked membrane. The porosity was calculated using the following equation **(S1)**;

$$\text{porosity } (\varepsilon) = \frac{(w_1 - w_0)}{\rho_s} \Big/ V_0 \times 100 \qquad \textbf{(S1)}$$

where w_1 and w_0 are the weights of polymer membranes dried and soaked in *n*-hexadecane, respectively, ρ is the density of n-hexadecane, and V_0 means the total volume consisting of the polymer and pores occupied by n-hexadecane.

Thermal diffusivity measurements (NETZSCH, LFA 447 NanoFlash) were conducted using an InSb sensor at 25 ^{o}C using a dense membrane in a through-plane direction following ASTM E1461. The thermal conductivity of the membranes was calculated using the following equation **(S2)**;

$$k_m = k_a \times \varepsilon + k_p \times (1 - \varepsilon) \qquad \textbf{(S2)}$$

where k_m, k_p and k_a are the thermal conductivities of membrane, polymer and the

8. DCMD test

The test apparatus for direct contact membrane distillation (DCMD) was purchased from Phillos Company (Korea). All DCMD tests were conducted using the Teflon cell, which has a 0.00181 m^2 active area (see **Fig. S6**).

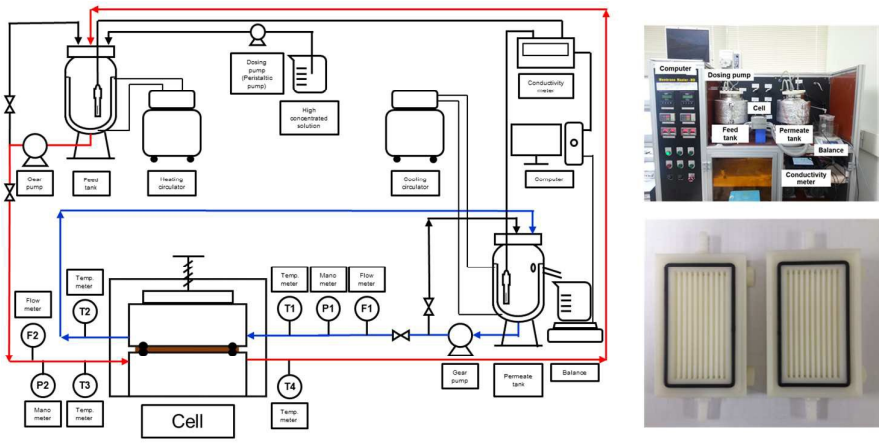

Fig. S6 DCMD apparatus and Teflon cell.

The feed temperature was controlled from 50 to 70 ^{o}C and was measured at the inlet and outlet of the cell. The permeate temperature was also checked at the inlet and outlet of the cell, and the average permeate temperature was fixed at 20 ^{o}C. All test were operated using a countercurrent flow type consisting of a hot feed and cold permeate flows through the bottom and top parts of the cell, respectively. During the test, the over-flow water from the permeate tank was collected on the beaker and the weight was recorded every 10 min. The conductivities of the feed and permeate tanks were also measured and sent to a computer every 10 min to calculate the salt rejection of the membrane. A dosing pump was employed to maintain the conductivity of the feed tank depending on the water flux of the membrane. The flow rates of feed and permeate were operated in a range of 0.5 to 2.0 ml min^{-1} with a 0.5 ml

min^{-1} step size. The water flux and salt rejection of all the membranes were observed at steady state at least 3 hr after changing the operating conditions.

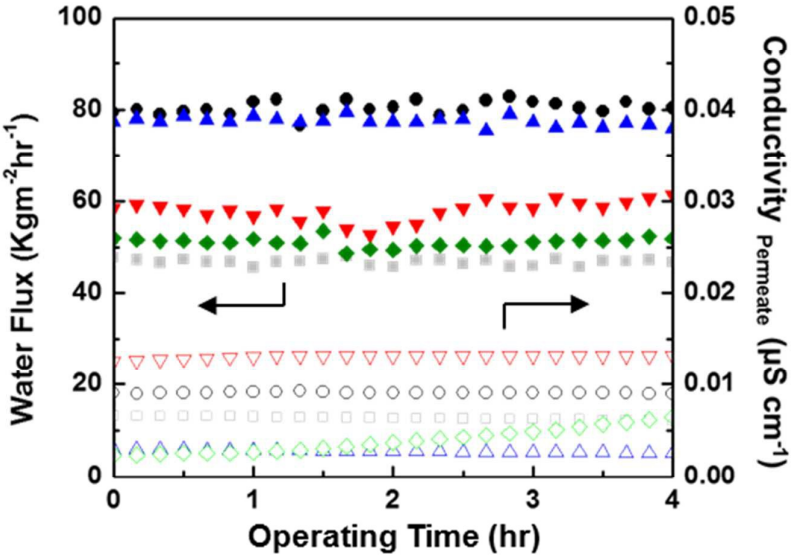

Fig. S7 Water flux and conductivity profiles of GVHP (■), P-PBO (▼), Up-PBO (●), NCM 1 (◆) and NCM 2 (▲) membranes for 4 hr using synthetic sea water (0.5 M NaCl aqueous solution) as a feed (70 °C) and D.I. water as a permeate (20 °C) at a flow rate of 2 L min^{-1}.

As shown in **Fig. S7**, all the membranes exhibited stable MD performance in terms of permeate conductivity. Among those, TR-NFM-1 and TR-NCM-2 exhibited high water flux with excellent salt rejection. Therefore, those membrane were used in a long term stability test.

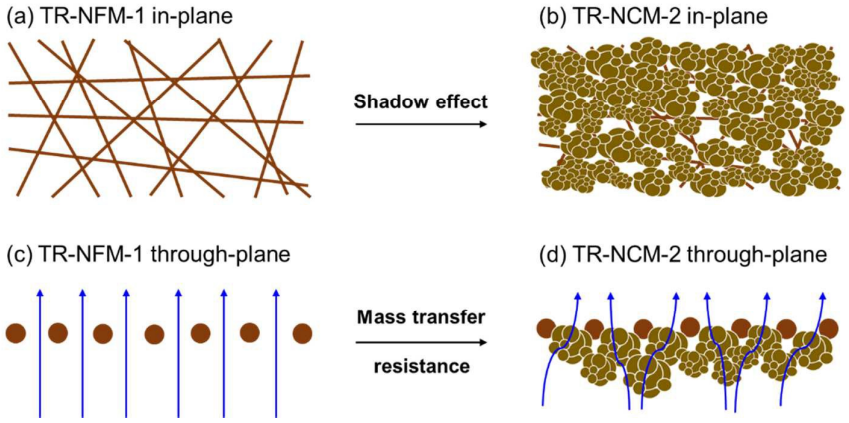

Fig. S8 Illustration of the surface and cross-section of TR-NFM-1 and TR-NCM-2.

Since TR-NCM-2 was coated with porous TR-PBOI particles, the particle coating layer induces a shadow effect to cause the performance difference between the TR-NFM-1 and TR-NCM-2, as shown in **Fig. S8**. As a result, although the particle coating certainly prevents the membrane from wetting, the shadow effect of the particles increased the mass transfer resistance through the coating layer lowering the membrane water flux. The shadow effect of the particles was already reported in the literatures,[7, 8] where the surface pores were blocked by the particles preventing water evaporation.

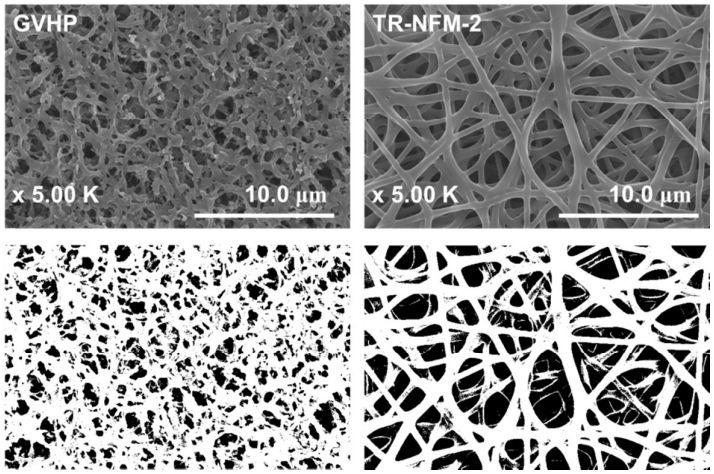

Fig. S9. SEM images and edited SEM images of GVHP and TR-NFM-2 to calculate the

surface porosity. The SEM images were edited by ImageJ program. The surface porosity of GVHP and TR-NFM-2 are 28.7 ± 2.88 and 38.9 ± 2.14 %, respectively.

The porosity (75 %), contact angle (120 °) and roughness (146 nm) of GVHP were higher than those (64 %, 100 ° and 69 nm) of TR-NFM-2. It can be deduced that GVHP membrane would have broader transfer channel for the water vapor, higher water curvature on the surface pores for evaporation of the water vapor, and lower temperature polarization (TP) from the induced turbulent flow compared to those of TR-NFM-2. On the other hand, the larger thickness (125 μm) and lower surface porosity (28.7 %, shown in **Fig. S9**) of GVHP lowered the water vapor transport through the membrane and reduced the effective area for the water vapor to evaporate than those (60 μm and 38.9 %) of TR-NFM-2, respectively (**Fig. S9**).

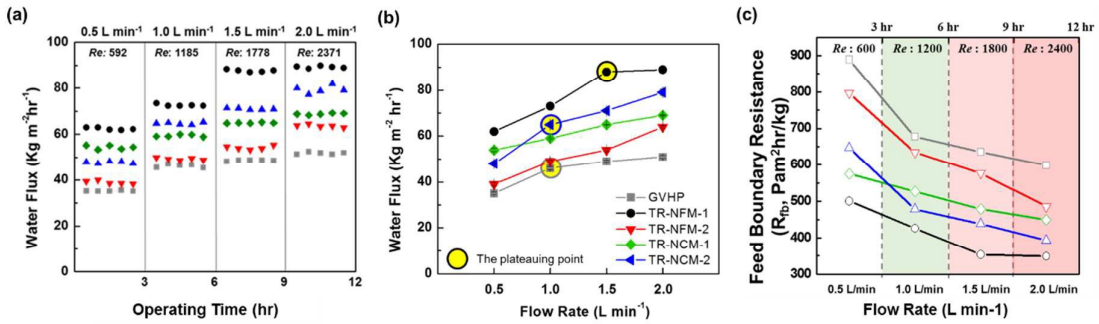

Fig. S10 The water flux (a) and (b), and feed boundary resistance profiles (c) of GVPH (■), TR-NFM-1 (●), TR-NFM-2 (▼), TR-NCM-1 (♦) and TR-NCM-2 (▲) according to different *Re* (600, 1200, 1800 and 2400) of flow rate.

As shown in **Fig. S10,** it is well accepted that increasing the crossflow velocity increases the *Re* number, creating more turbulence on the membrane surface which reduces the temperature polarization, improving the observed flux. Generally, the higher the surface roughness, the higher the turbulence effect. Importantly, the flux improvement with the

increasing *Re* number typically plateaus off in the form of logarithmic function.[9-11] Hence, the change in flux with change in *Re* ($\frac{dJ}{dRe}$) becomes lower with higher *Re*. There is a larger flux improvement when the crossflow velocity increased from 0.5 to 1.0 L min^{-1} compared to the flux improvement from 1.5 to 2 L min^{-1}, due to the aforementioned logarithmic trend. As can be seen in **Fig. S10c**, the flux values of TR-NFM-2 (red) and TR-NCM-1 (green) increases proportionally to flow rate (*Re*). On the other hand, the flux data for TR-NFM-1 (black), TR-NCM-2 (blue) and GVHP (gray) exhibited clear plateauing points, with TR-NFM-1 showing the plateauing point at higher flow rate. In the tested range of flow rates, TR-NFM-2 and TR-NCM-1 did not show visible plateauing points. Such trend, of course, is a function many factors including the surface morphology of the membranes.

For instance, the surface roughness values of TR-NCM-2 (133 nm) and GVHP (146 nm) were higher than that of TR-NFM-1 (101 nm). Therefore, the plateauing points of TR-NCM-2 and GVHP were lower than that of TR-NFM-1. On the other hand, TR-NFM-2 and TR-NCM-1 did not show a plateauing point in the tested range. Since TR-NFM-2 has low surface roughness (69 nm) and high thermal conductivity (0.122 W m^{-2} K^{-1}), we suspect the plateauing point for TR-NFM-2 would exist at a flow rate higher than 2.0 L min^{-1}. On the other hand, TR-NCM-1 had high surface roughness, the low thermal conductivity with small and narrow surface pore size distribution, and we suspect lower plateauing point at a flowrate lower than 0.5 L min^{-1}.

The water flux difference was also hopefully explained by the feed boundary resistance (R_{fb}) which represents effect of flow rate on temperature polarization phenomena at feed was derived using following equations:[12, 13]

$$R_{fb} = \frac{P_f - P_{fm}}{J_w} \quad \textbf{(S3)}$$

where P_f is the vapor pressure at bulk feed, P_{fm} is the vapor pressure at feed membrane surface and J_w is the water flux.

Because the R_{fb} was calculated with considerations of fluid dynamics and heat transfer models at feed, consequently, the R_{fb} could represent the relative effects of temperature polarization at feed as well as the membrane properties for the MD performance. Therefore, the R_{fb} would be adequately explain the difference of observed water flux with a collectively insight of the cell design, fluid dynamics, heat transfer and surface morphologies of the membranes.

The vapor pressure was calculated by Antoine equation:[12, 13]

$$P_i = \exp\left(23.238 - \frac{3841}{T_i - 45}\right), (i = f, fm) \quad \textbf{(S4)}$$

where T_f and T_{fm} are the temperature at bulk feed and feed membrane surface, respectively.

The T_{fm} can be derived from the energy balance at steady state.[12, 13]

$$\mathrm{Q} = Q_f = Q_m = Q_p \quad \textbf{(S5)}$$

$$= h_f(T_f - T_{fm}) = h_m(T_{fm} - T_{pm}) = h_p(T_{pm} - T_p) \quad \textbf{(S6)}$$

$$T_{fm} = T_f - \frac{(T_f - T_p)\frac{1}{h_f}}{\frac{1}{h_m} + \frac{1}{h_p} + \frac{1}{h_f}} \quad \textbf{(S7)}$$

where Q_i is the heat flux at feed, membrane and permeate at steady state, respectively, and the T_{fm} can be calculated from **eqn (S7)**.

The heat transfer coefficients of membrane, feed and permeate were calculated by followed equations:

$$h_m = \frac{k_m}{\delta} \quad \textbf{(S8)}$$

$$h_i = \frac{Nu_i k_i}{D_h}, (\mathrm{i} = \mathrm{f}, \mathrm{p}) \quad \textbf{(S9)}$$

where the h_m, h_p and h_f are the heat transfer coefficient of membrane, permeate and feed, respectively, the km is the thermal conductivity of the membrane and δ is the membrane thickness, and the D_h is the hydraulic diameter.

$$Nu_i = 0.13\, Re^{0.64} Pr^{0.38}, (Re < 2100) \quad \textbf{(S10)}$$

$$Nu_i = 0.23 Re^{0.8} Pr^{0.33}, (Re > 2100) \quad \textbf{(S11)}$$

$$Re = \frac{\rho v D_h}{\mu} \quad \textbf{(S12)}$$

$$Pr = \frac{C_p \mu}{k} \quad \textbf{(S13)}$$

where Nusselt (*Nu*), Reynolds (*Re*) and Prandtl (*Pr*) numbers were used for calculate heat transfer coefficient at feed and permeate, respectively, the ρ is the density of the fluid, the υ is the mean velocity of the fluid, the μ is the dynamic viscosity of the fluid, and the k is the thermal conductivity.

The feed boundary resistance decreased with increasing *Re* number (higher flow rates). It can also be seen that the change in the boundary resistance with increasing *Re* number is different between the membranes. Generally, the change in the boundary resistance with respect to the feed flowrate ($\frac{dR_{fb}}{dF}$) became smaller at higher *Re*. Therefore, there was bigger change in the water flux in the lower range of *Re* compared with the change in the higher range of *Re*. In addition, the change in the boundary resistance ($\frac{dR_{fb}}{dF}$) was different between

the membranes, as the membranes exhibit different surface morphologies. In the case of TR-NFM-1, ($\frac{dR_{fb}}{dF}$) only became smaller at higher flow rates, whereas ($\frac{dR_{fb}}{dF}$) for TR-NCM-2 got smaller at lower flow rates. The main difference between the TR-NCM-2 and TR-NFM-1 membranes is the presence of TR particle coating layer. Since the surface pore size, surface porosity and roughness which can all influence the evaporation of water molecules as well as the feed boundary resistance. Therefore, we carefully conclude that the flow rate of feed solution has bigger effect to the water flux of TR-NFM-1 due to the lower feed boundary resistance.

After long-term test, the cross-section of TR-NCMs was observed by SEM. As shown in **Fig. S11**, the TR-PBOI particles and nanofibers were still fused together.

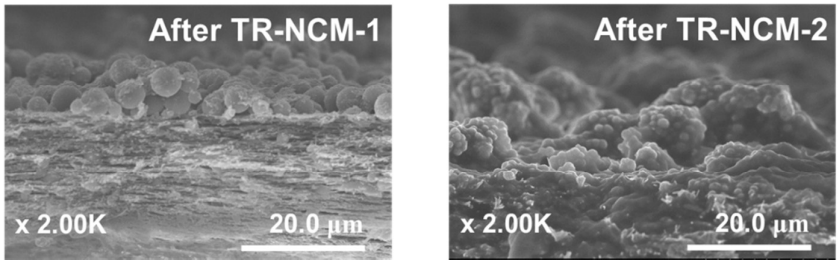

Fig. S11 SEM images of (a) TR-NCM-1 and (b) TR-NCM-2 after long-term test.

The chemical stability test of TR-NFM-1 was conducted in organic solvents, acid and base solution (NMP, DMAc, DMSO, H_2SO_4 and 3 M KOH aqueous solution). As shown in **Fig. S12**, the samples of TR-NFM-1 (2 x 5 cm^2) which were immersed in several types of harsh organic solvents, acid and base solution does not dissolve in any solution after three months. After washing out the solvents, any weight change of the membranes was not observed, indicating that the membranes can withstand chemical cleaning conditions.

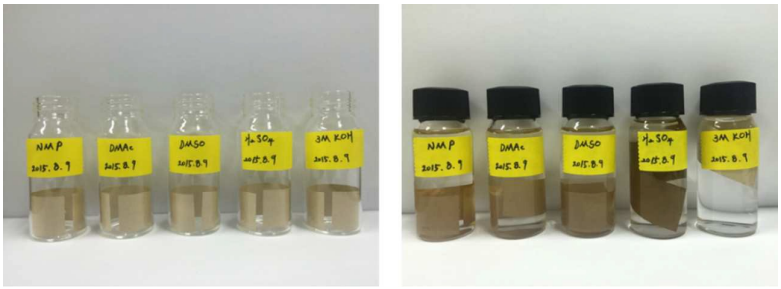

Fig. S12 Chemical stability test in organic solvent, acid and base solutions. (NMP, DMAc, DMSO, concentrated sulfuric acid (H_2SO_4) and 3 M KOH aqueous solution for three months.

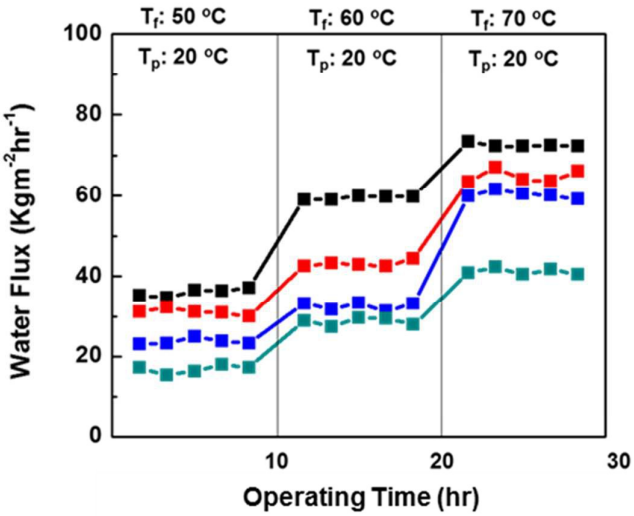

Fig. S13 The water flux profile of TR-NFM-1 was investigated using different feed concentration (0.5 M (■), 1.0 M (■), 3.0 M (■), and 5.0 M (■) of NaCl aqueous solution) with 1 L min^{-1} of flow rates.

9. MCr test

Membrane crystallization (MCr) testing was also conducted using the same apparatus (**Fig. S6**). The feed used was a 352.6 g L^{-1} NaCl aqueous solution at 50 ^{o}C. D.I. water was used as a permeate at 20 ^{o}C. After pre-heating both feed and permeate solutions, the solutions were circulated in counter current mode with a 1 L min^{-1} flow rate. Then, 5 ml samples were collected at the bottom of the feed tank, and these were observed with an optical microscope (BX51-P, Olympus, Japan). Aliquot samples were sandwiched between slide glasses and were

observed at x20 magnification of the lens (MPlanFL series, Olympus, Japan) using the OM. The surface of the membranes were observed with SEM right after finishing the MCr operation; in order to prepared these samples, an excess solution on the membrane surface was removed and dried in a convection oven at 70 ^{o}C overnight. The crystal size and distribution were measured using the imageJ program for more than 100 crystals.

After 3 hr of operation, NaCl crystals 123 ± 22 μm in size, which were produced by TR-NFM-1, were obtained as shown in **Fig. S14**.

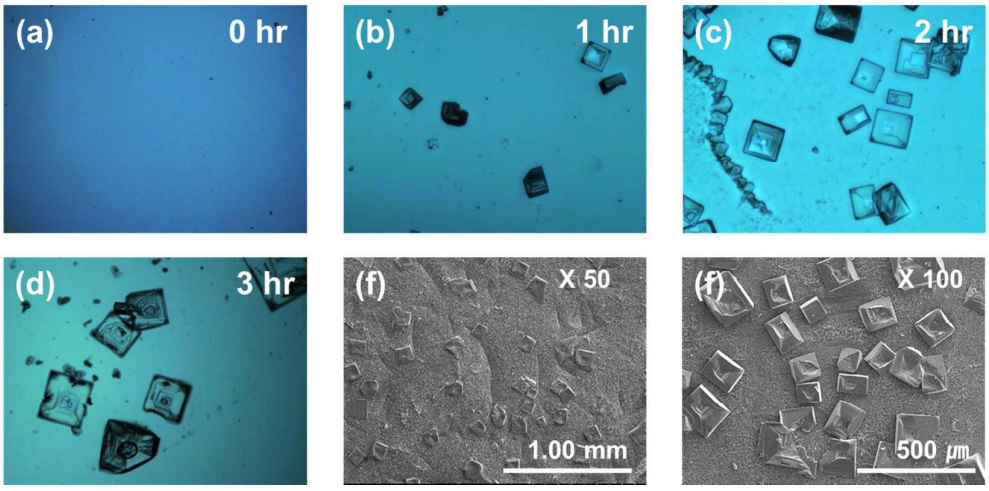

Fig. S14 (a-d) Optical microscopy and (e and f) SEM images of NaCl crystals which were obtained by the MCr test of TR-NFM 1 using a 352.6 g L^{-1} NaCl aqueous solution and D.I. water as feed (50 ^{o}C) and permeate (20^{o}C) solutions, respectively with flow rates of 1 L min^{-1}.

TR-NFM-1 and TR-NFM-2 were also tested using a 352.6 g ml^{-1} NaCl aqueous solution as feed (50 ^{o}C) and D.I. water as permeate (20 ^{o}C) with different flow rates (1 L min^{-1} and 2 L min^{-1}). Aliquots of samples for optical microscopy analysis were obtained at 14 h and at the end of operation. The optical microscopy images were analyzed using the ImageJ program. To estimate the size distribution, at least 100 crystals were measured.

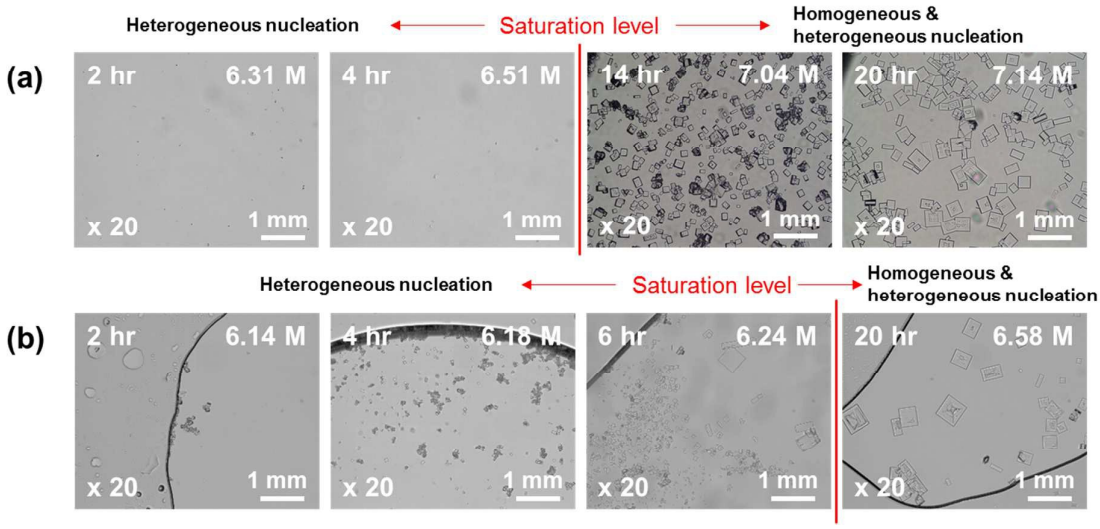

Fig. S15 The optical microscopy images of (a) TR-NFM-1 and (b) TR-NFM-2 according to operation time using 352.6 g L^{-1} NaCl aqueous solution as the feed (50 ^{o}C) and D.I. water as the permeate (20 ^{o}C) with 2 L min^{-1} of flow rate. The saturation concentration of the NaCl aqueous solution was 6.47 M at 50 ^{o}C.

To confirm the presence of heterogeneous nucleation, we have conducted further experiment using TR-NFM-1 and TR-NFM-2 membranes as they are most likely to show heterogeneous nucleation. The membranes were tested using 352.6 g L^{-1} of NaCl aqueous solution (near saturation concentration) as the feed (50 ^{o}C) and deionized water as the permeate (20 ^{o}C). Aliquot feed samples were taken and observed using optical microscope at 1 hr interval until the solution reached the saturation level. As shown in **Fig. S15**, in the case of the TR-NFM-2 with $\Delta G^{*}_{het}/\Delta G^{*}_{hom}$ value of **0.65**, salt crystals are clearly visible below the saturation level, suggesting they have formed via heterogeneous nucleation. On the other hand, TR-NFM-1 ($\Delta G^{*}_{het}/\Delta G^{*}_{hom}$ value of **0.88)** did not show salt crystals until the solution became saturated. Therefore, we believe for stable MD performance, the membrane $\Delta G^{*}_{het}/\Delta G^{*}_{hom}$ value should be as close to unity as possible for DCMD process. In addition, in order to prevent local

supersaturation, the membrane should possess high LEP to withstand turbulent feed flow rates.

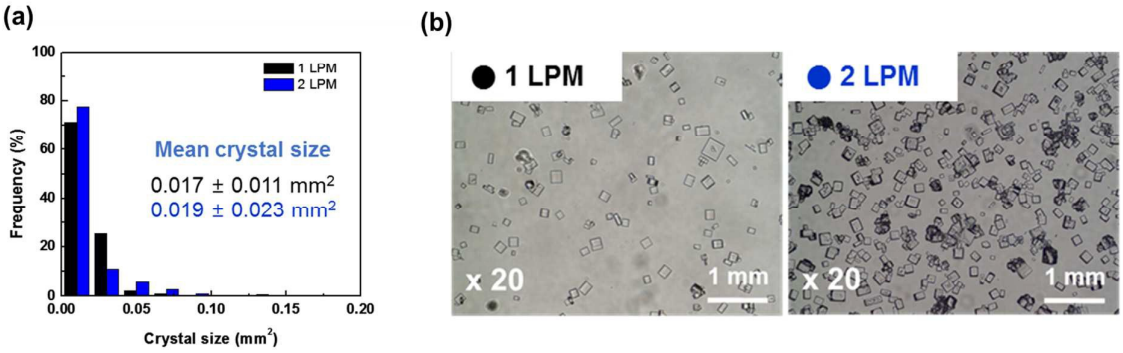

Fig. S16 (a) Crystal size distribution and (b) optical microscopy images of operation at different flow rates: 1 L min^{-1} (●) and 2 L min^{-1} (●) after 14 h operation with TR-NFM-1.

TR-NFM-1 was also used to produce Na_2SO_4 crystals using a 184.6 g L^{-1} Na_2SO_4 aqueous solution (feed, 50 ^oC) and D.I. water (permeate, 20 ^oC) as shown in **Fig. S17**. Aliquots of crystallizing solutions for optical microscopy measurement were sampled after 500 and 530 min of operation and were analyzed.

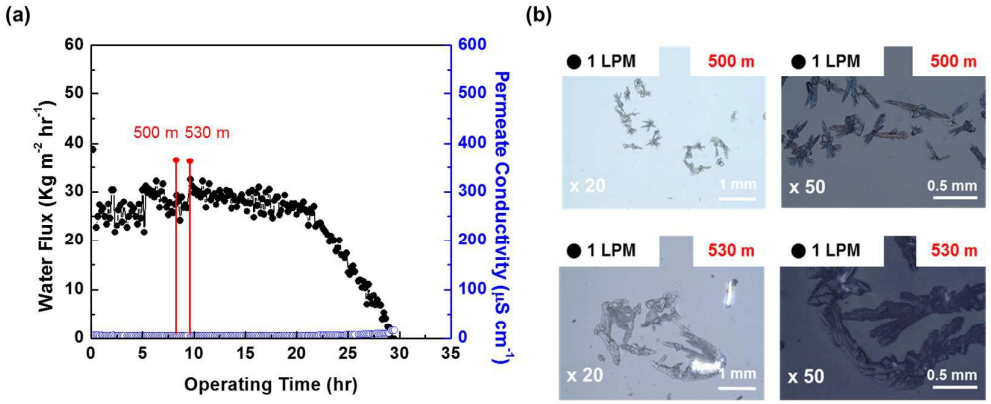

Fig. S17 (a) The water flux and permeate conductivity of TR-NFM-1 were measured with a 184.6 g L^{-1} Na_2SO_4 aqueous solution as feed (50 ^oC) and D.I. water as permeate (20 ^oC) at a flow rate of 1 L min^{-1}. (b) Na_2SO_4 crystals were measured using optical microscopy after 500 and 530 min of MCr operation.

10. References

1. L. D. Tijing, J.-S. Choi, S. Lee, S.-H. Kim and H. K. Shon, *J. Membr. Sci.*, 2014, **453**, 435-462.
2. X. Li, C. Wang, Y. Yang, X. Wang, M. Zhu and B. S. Hsiao, *ACS APPl. Mater. Inter.*, 2014, **6**, 2423-2430.
3. S. H. Han, N. Misdan, S. Kim, C. M. Doherty, A. J. Hill and Y. M. Lee, *Macromolecules*, 2010, **43**, 7657-7667.
4. M. J. Lee, J. H. Kim, H. S. Lim, S. Y. Lee, H. K. Yu, J. H. Kim, J. S. Lee, Y. K. Sun, M. D. Guiver, K. D. Suh and Y. M. Lee, *Chem. Commun.*, 2015, **51**, 3474.
5. A. Pongpeerapat, C. Wanawongthai, Y. Tozuka, K. Moribe and K. Yamamoto, *Int. J. Pharm.*, 2008, **352**, 309-316.
6. J. Y. Xiong, X. Y. Liu, S. B. Chen and T. S. Chung, *J. Phys. Chem. B*, 2005, **109**, 13877-13882.
7. Y. Liao, R. Wang and A. G. Fane, *J. Membr. Sci.*, 2013, **440**, 77-87.
8. Y. Liao, R. Wang and A. G. Fane, *Environ. Sci. Technol.*, 2014, **48**, 6335-6341.
9. F. Laganà, G. Barbieri and E. Drioli, *J. Membr. Sci.*, 2000, **166**, 1-11.
10. T. Y. Cath, V. D. Adams and A. E. Childress, *J. Membr. Sci.*, 2004, **228**, 5-16.
11. A. Razmjou, E. Arifin, G. Dong, J. Mansouri and V. Chen, *J. Membr. Sci.*, 2012, **415-416**, 850-863.
12. S. Srisurichan, R. Jiraratananon and A. Fane, *J. Membr. Sci.*, 2006, **277**, 186-194.
13. J. Phattaranawik, R. Jiraratananon and A. G. Fane, *J. Membr. Sci.*, 2003, **212**, 177-193.